Journal of the European Ceramic Society **17** (1997) 1501–1511

PII: S0955-2219(97)00005-8
0955-2219/97/$17.00

Influence of Stoichiometry on Fracture Behaviour of Magnesium Aluminate Spinels at 1200°C

C. Baudín & P. Pena

Instituto de Cerámica y Vidrio, 28500 Arganda del Rey (Madrid), Spain

(Received 23 July 1996; revised version received 26 November 1996; accepted 2 December 1996)

Abstract

The mechanical behaviour at 1200°C of one stoichiometric and two alumina rich polycrystalline magnesium aluminate spinels is studied. Similar microstructures have been obtained for both spinel compositions. Lattice parameters have been determined and related to the solid solution stoichiometry for all materials. Microstructures have been characterized by scanning electron microscopy. Fracture toughness measurements at 1200°C as a function of strain rate and observations of polished and fracture surfaces have been performed. Relationships between fracture behaviour and microstructure and solid solution composition have been established In spite of similarities between microstructure (porosity, grain size), two differentiated fracture behaviours as a function of composition have been found. The stoichiometric spinel presents intergranular fracture and crack bridging at all strain rates used, whereas high alumina spinels show mostly transgranular fracture. © 1997 Elsevier Science Limited.

1 Introduction

Magnesium spinel ($MgAl_2O_4$) offers a desirable combination of properties—high melting point, potentially high strength, high resistance to chemical attack and low electrical losses which make it important as a high refractory, electroinsulating and structural material with application in metallurgical, electrotechnical, and radiotechnical industries.

In previous work[1] the mechanical and elastic behaviour from room temperature up to 1300°C of a conventionally sintered non-translucent polycrystalline stoichiometric magnesium aluminate spinel ($MgAl_2O_4$) was studied. Non-linear load–deflection relationships during fracture were found from 800°C, with a strong dependence of fracture toughness on temperature and strain rate. Apparent K_{IC} values at 1200°C increased as strain rate decreased and a mechanism of crack tip yielding via defect rearrangement during fracture was proposed to explain this fracture behaviour.

Alumina has a wide solid solubility in magnesium aluminate spinel. Depending on the temperature, single phase spinel is formed in a wide range of compositions. At the sintering temperature used in this work, 1750°C, $MgO{\cdot}xAl_2O_3$ solid solution has been reported for $x = 1$–$2{\cdot}5$.[2]

Panda and Raj[3] determined the time–temperature–transformation (ttt) curves for alumina precipitation in a $MgO{\cdot}2Al_2O_3$ polycrystalline material and found a C-shape typical of phase transforming systems in which phase transformation is nucleation limited.

Fundamental studies on mechanical behaviour and press forging of Verneuil-grown single crystals of alumina rich spinels have been reported.[4–8] It is generally agreed that the excess of octahedral cation vacancies in non-equimolar compositions is responsible for the enhanced plastic deformation when the molar ratio of alumina to magnesia is greater than unity.[4,5,8]

Panda *et al.*[8] have studied the high temperature deformation under load of a polycrystalline $MgO{\cdot}2Al_2O_3$ spinel and observed that this supersaturated spinel showed maximum superplasticity in tests performed at low strain rates and close to the solvus temperature. This superplasticity was accompanied by dynamic precipitation of αAl_2O_3, as observed by scanning electron microscopy (SEM), and enhanced ductility continued beyond the time when all supersaturated alumina should have precipitated. The inference of these authors was that dynamic precipitation leads to some decrease in the flow stress. Superplasticity of $MgO{\cdot}2Al_2O_3$ polycrystals at temperatures close to the solvus has also been reported by Maguire and Gentilman;[9] these authors did not detect any alumina precipitation by optical microscopy or X-ray diffraction (XRD).

This paper describes the fracture behaviour of one stoichiometric and two non-stoichiometric conventionally sintered non-translucent polycrystalline spinel materials at 1200°C. This temperature, at which plastic deformation during fracture of a stoichiometric material was reported by the present authors,[1] is far from the solvus temperature of the non-stoichiometric compositions (~1650°C). Similar microstructures for the stoichiometric and one of the non-stoichiometric spinels have been developed in order to check the intrinsic effect of non-stoichiometry on deformation under load of the materials.

The effect of strain rate on fracture behaviour has been studied in order to account for the possible effects of plastic phenomena during fracture.

2 Experimental Procedure

A stoichiometric commercial spinel $MgAl_2O_4$ powder (Baikalox, USA) and a Bayer alumina (Alcoa, CT 3000 SG, USA) have been used as starting materials. The characteristics of these powders are shown in Table 1. The size of the agglomerate for spinel, measured by sedigraph (5000 ET, Micromeritics USA) in ethyl alcohol is 7·5 μm.

Table 1. Characteristics of powders used in this study

	Alumina	*Spinel*
Ignition loss (wt%)	0·5	1·11
SiO_2 (wt%)	0·0	0·16
Al_2O_3 (wt%)	99·6	71·9
Fe_2O_3 (wt%)	0·03	0·12
TiO_2 (wt%)	0·001	0·004
Na_2O (wt%)	0·12	0·005
K_2O (wt%)	n.d.	0·011
CaO (wt%)	0·04	0·02
P_2O_5 (wt%)	n.d.	0·10
MgO (wt%)	0·01	26·0
Specific surface area[a] (m^2/g)	8	5
Crystallite size (μm)	0·5	0·4

[a]Determined by BET (Monosorb MS-13, Quantachrome, USA)
n.d. = not determined.

The processing paths summarized in Table 2 were used to prepare one stoichiometric (SP; $MgO{\cdot}xAl_2O_3$, $x \sim 1$) and two alumina rich (SPA-I, SPA-II; $MgO{\cdot}xAl_2O_3$, $x \sim 2$) spinel materials from the powders described in Table 1.

Debye–Scherer powder diffraction patterns were obtained using an X-ray diffraction powder camera (Siemens D-5000, Germany) with CuK_α X-ray (Ni filtered) at 50 kV and 30 mA. XRD patterns were indexed in accordance with the powder diffraction file data card of spinel.[10] The precise lattice parameters were determined using the XRD lines corresponding to Bragg angles greater than $\pi/3$ and Si as internal standard.

The actual molar composition of the obtained materials, x, was calculated from the determined lattice parameters using the following relation:[8]

$$x = (0{\cdot}86109 - a_0)/(3a_0 - 2{\cdot}37195) \qquad (1)$$

where a_0(nm) is the lattice parameter of the spinel solid solution. The density of the sintered compacts was determined by the Archimedes' method using distilled water.

Microstructural characterization was performed by SEM (Zeiss DSM 950, Germany), on polished and chemically etched (phosphoric acid at 185 ± 5°C—6 min) surfaces. Microanalysis of different spinel grains was performed by SEM–EDX. The average grain size of the samples was calculated, assuming spherical grains, on two-dimensional cross-sections using the following relation:

$$d = 1{\cdot}56\, d_1 \qquad (2)$$

where d is the corrected grain size and d_1 is the average grain size obtained from the linear intercept method.

Room temperature Young's modulus was determined from the resonance frequency of bars (4 mm × 3 mm × 50 mm) using a commercial apparatus (Grindosonic, Belgium).

Toughness (SENB) was determined at 1200°C on diamond machined samples (4 mm × 6 mm × 50 mm) with diamond-sawn notches of 3 mm length and 25 μm thickness. Tests were carried

Table 2. Processing routes used to prepare studied materials

	SP	*SPA-I*	*SPA-II*
Powder processing	Attrition milling: 4 h, ethyl alcohol, alumina balls. Drying: 75°C, 24 h. Sieving: 65 μm.	Attrition milling: 2 h, isopropyl alcohol, alumina balls. Drying: 75°C, 24 h. Sieving: 65 μm.	Attrition milling: 4 h, ethyl alcohol, alumina balls. Drying: 75°C, 24 h. Sieving: 65 μm
Pressing	Cold isostatic pressing at 200 MPa		
Sintering (heating/cooling rates 2°C—min)	1750°C—2 h	1750°C—2 h	1750°C—2 h

out using a four-point bending device (Instron, G.B; 40–20 mm, outer–inner spans) made of Al_2O_3 and cross-head speeds ranging from 0·005 mm/min up to 2·5 mm/min. Apparent K_{IC} values were calculated using ASTM STP601,[11] taking as notch sizes the sizes of the diamond-sawn notches measured in a reflected light microscope. Apparent K_{IC} reported values are the average of four tests. All fracture surfaces were observed by SEM.

Reported uncertainty values for Young's modulus and apparent toughness are standard deviations.

3 Results

3.1 Mineralogical and microstructural characterization

XRD spectra of all the obtained materials showed only the diffraction lines corresponding to spinel. The characteristics of the obtained materials are summarized in Table 3. Density and Young's modulus values are almost the same for all materials. Lattice parameters of the samples with alumina excess are lower than those corresponding to the stoichiometric spinel. All calculated compositions correspond to alumina rich spinels: one of them very close to the stoichiometric $MgO{\cdot}Al_2O_3$, SP, and the other two close to $MgO{\cdot}2Al_2O_3$, SPA-I and SPA-II.

Figure 1 shows general views (SEM) of the microstructures of the sintered samples. Observed microstructures are modified by the chemical etching needed to reveal grain boundaries which partially dissolves spinel grains as can be seen by comparison between the strongly etched polished surfaces of Fig. 1 and the non-etched or slightly etched polished surfaces of Fig. 2. The microstructure of SPA-I (Fig. 1(b)) is bimodal with high density large grains (~40 μm) surrounded by a low density matrix. Microstructures of SP and SPA-II (Fig. 1(a,c)) are made of a single distribution of large grains (~70 μm) with intragranular porosity and surrounded by pore chains.

In Fig. 3 the two microstructural features of SPA-I can be observed in detail. No differences in composition (EDX) between the large and small particles are found. Small particles in the matrix (Fig. 3(b)) have an average diameter of $1{\cdot}4 \pm 0{\cdot}6$ μm.

High magnification micrographs (SEM) of SP and SPA-II microstructures are shown in Fig. 4. Two different features are observed at the grain boundaries: straight grain to grain junctions and pore chains. Intragranular porosity is present in both samples and pores located in the bulk of the grains are smaller than those located close to or at the grain boundaries.

3.2 Mechanical characterization

The fracture of materials SPA-I and SPA-II was unstable at all cross-head speeds used whereas SP samples tested at $v < 2{\cdot}5$ mm/min showed stable fracture behaviour.

For all materials, the calculated stress intensity factors at the onset of fracture were strongly dependent on strain rate and cannot be considered as K_{IC} values; in the following they will be called 'K_{IC}'.

Values of 'K_{IC}' at 1200°C as a function of the cross-head speed for the three materials are shown in Fig. 5. For SP these values were calculated from the maximum loads recorded during testing previous to the controlled fracture of the samples. For the alumina rich materials (SPA-I, SPA-II), a minimum in toughness is observed for the lowest cross-head speed, 'K_{IC}' being constant for higher speeds. The calculated stress intensity factors at the onset of fracture for SP increase as the loading rate increases.

No special features were observed in any of the fracture surfaces of toughness samples tested at 1200°C using the largest loading rate (2·5 mm/min). Conversely, in the samples tested at lower rates different habits of fracture as a function of distance to the notch existed.

In the low magnification micrographs of SPA-I fracture surfaces, no differentiated zones were observed and all surfaces presented the same features as the one shown in Fig. 6(a). When higher magnifications were used for all samples, mostly transgranular fracture was observed close to the notch (Fig. 6(b)) as well as at the centre of the samples (Fig. 6(c)).

In all SPA-II fracture surfaces of samples tested at 0·005 mm/min, differentiated zones close to the notch were observed even for the lowest magnification. Fig. 7 shows one of these surfaces. Close to the notch a semielliptical area (Fig. 7(a)) in

Table 3. Characteristics of studied materials

	SP	*SPA-I*	*SPA-II*
Lattice parameter (nm)	0·80800 ± 0·00005	0·8008 ± 0·0001	0·8009 ± 0·0001
Calculated molar composition, x, ($MgO{\cdot}xAl_2O_3$)	x=1·019 ± 0·003	x = 1·98 ± 0·01	x = 1·96 ± 0·01
Density (g/cm^3)	3·46 ± 0·03	3·45 ± 0·03	3·46 ± 0·02
Young's Modulus (GPa)	251 ± 13	256 ± 11	257 ± 10

which intergranular fracture takes place (Fig. 7(b)) is clearly observed. Out of this region mostly transgranular fracture occurs (Fig. 7(c)). In the samples tested at higher strain rates fracture was mainly transgranular and the surfaces showed the same features as those shown in Fig. 7(c). Load–cross-head displacement curves recorded during toughness tests for SP are depicted in Fig. 8. When the highest cross-head speed was used, typical unstable fracture occurred and 'K_{IC}' was the highest of all values obtained using this speed (Fig. 5). For the tests performed at 0·05 and 0·005 mm/min, fracture was partially stable (Fig. 8) and the fracture surfaces were held together after the test. All fracture surfaces of SP samples presented intergranular fracture along the porous boundaries of the large spinel grains shown in Fig. 1(a). Figures 9 and 10 show polished surfaces cut perpendicular to the notch of SP toughness samples tested at medium and low rates in which the crack path is observed. Close to the notches

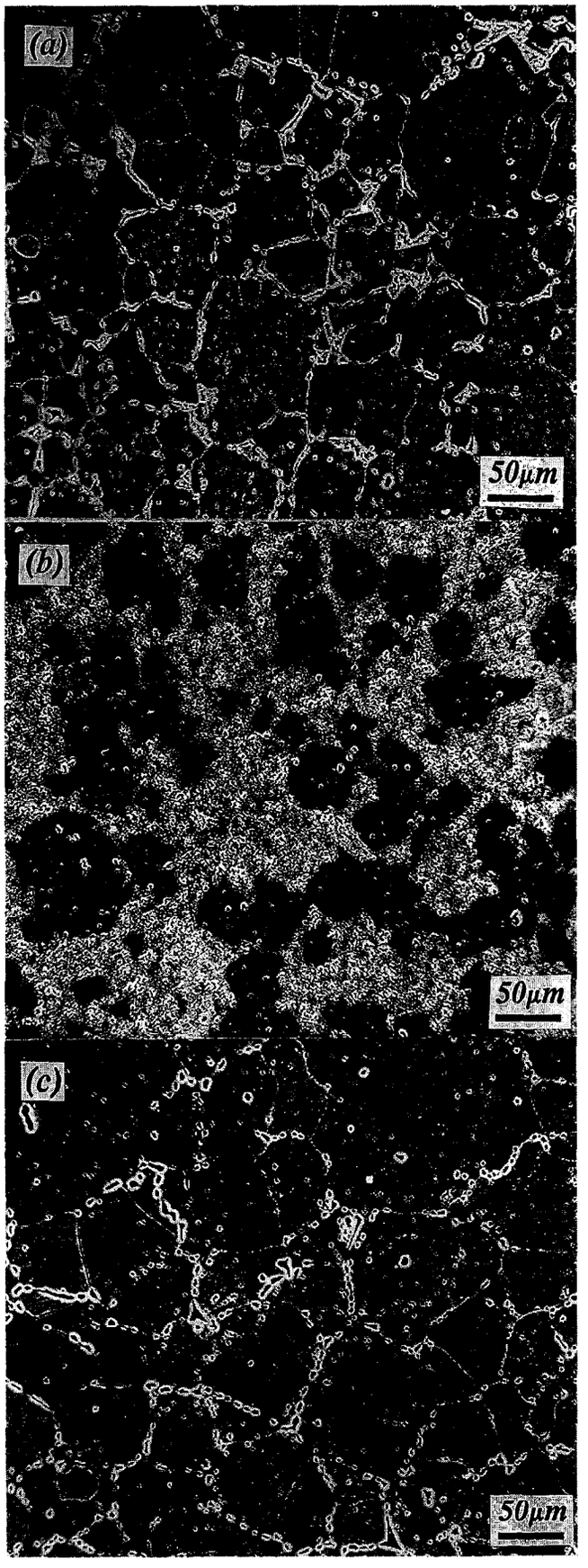

Fig. 1. Microstructures of studied materials. SEM micrographs of polished and chemically (H_3PO_4—6 min) etched surfaces. (a) SP, (b) SPA-I and (c) SPA-II.

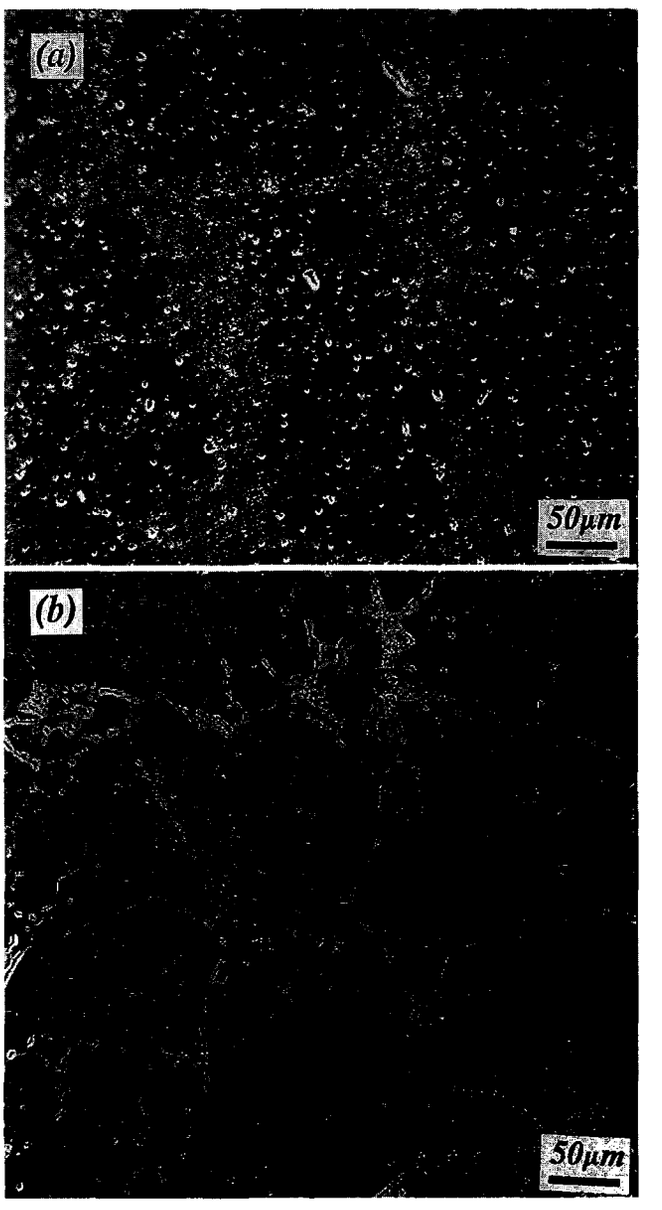

Fig. 2. SEM micrographs of polished surfaces. The effect of different etchings can be observed by comparison to Fig. 1. (a) SPA-I. Non-etched polished surface. (b) SP. Chemically etched (H_3PO_4—3 min).

damage distinct from the main crack occurs (Fig. 9) and secondary cracking and bridging effects are observed before the main crack reaches the end of the bars (Fig. 10).

4 Discussion

The obtained XRD results (Table 3) demonstrate that the three studied materials can be divided in two groups in terms of composition ($MgO{\cdot}xAl_2O_3$): one almost stoichiometric spinel, SP, and two alumina rich spinels, SPA-I and SPA-II with $x \approx 2$ (Table 3). The fact that the calculated solid solution of SPA-I and SPA-II coincides with the intended one in the starting mixture, and that no diffraction line for Al_2O_3 was found in any of the samples, reveals that these materials are made only of supersaturated solid solutions.

The room temperature dynamic Young's modulus (Table 3) of the stoichiometric spinel (SP) is the same as that determined by Stewart and co-workers[2,12] for a stoichiometric hot pressed spinel. The fact that variations in density and Young's modulus values of the three materials (Table 3) are inside the experimental variability in spite of the differences in chemical composition and lattice parameter can be related to the high porosity observed in the microstructures (Figs 1 and 2) as porosity is a determining parameter for Young's modulus values.

No impurity concentration, at the level of resolution employed, or singular large defects were found in any of the studied materials. The milling

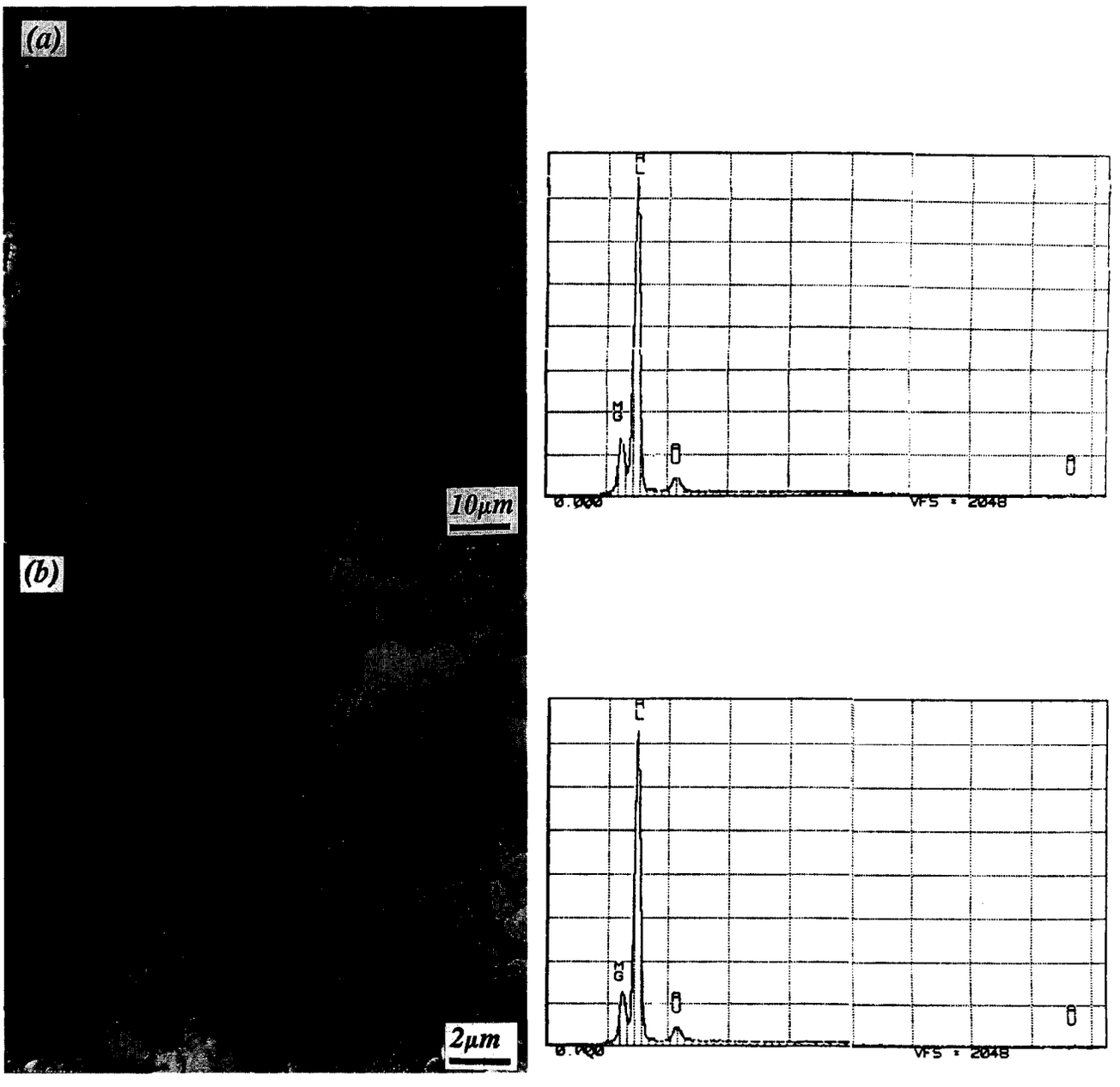

Fig. 3. SEM micrographs and corresponding EDX analysis of polished and chemically etched (H_3PO_4—6 min) surfaces of SPA-I. (a) Highly dense large particles. Trapped pores inside the grain and advanced stages of pore trapping at the grain boundaries are observed. (b) Small particles in the low density areas.

processes lead to a homogeneous distribution of impurities and to the breakdown of aggregates present in the starting spinel powder. Impurities in these materials (Table 1) must be uniformly distributed, forming spinel solid solutions (iron oxide) or thin amorphous phases along grain boundaries (silica, lime) as reported by Chiang and Kingery[13] for polycrystalline spinels prepared from the same kind of starting powders.

SPA-I presents a bimodal microstructure consisting of large (~40 μm) grains uniformly distributed in a low density and fine grained (~1·5 μm) matrix. Large grains have been formed by exaggerated grain growth, as can be deduced from Fig. 3(a) in which trapped pores and advanced stages of pore trapping are observed. This kind of microstructure is produced by the differential sintering of uniformly distributed agglomerates originating from the milling media (isopropyl alcohol) in the starting powder prior to sieving.

The two materials made from starting powders attrition milled in ethyl alcohol (SP and SPA-II, Table 2) have the same kind of microstructure (Fig. 1(a,c)) in which pore chains surround large (~60 μm) spinel grains with intragranular porosity. This kind of microstructure is also determined by the initial processing of the powders since the size of the spinel grains is the same as that of the sieve holes (65 μm). A number of necks exist between two large grains forming the mentioned pore chains. Intragranular porosity might be due to a combination of initial porosity inside the granules formed during sieving and non-stoichiometry defects inherent to spinel materials.

All materials studied here have lower apparent toughness values when low strain rates are used (Fig. 5), which is the kind of behaviour shown by materials in which subcritical crack growth takes place at low loads prior to fracture. The real size of the notches at the onset of fast fracture for samples in which subcritical crack growth occurs is larger than the size of the diamond-sawn notches. In materials SPA-I and SPA-II apparent toughness values are a minimum for the lowest speed and stable from 0·05 mm/min. In SPA-II fracture surfaces of samples tested at 0·005 mm/min intergranular fracture occurs in areas located close to the notches (Fig. 7(a,b)). These areas are the subcritical crack growth zones that weaken the samples prior to complete failure.

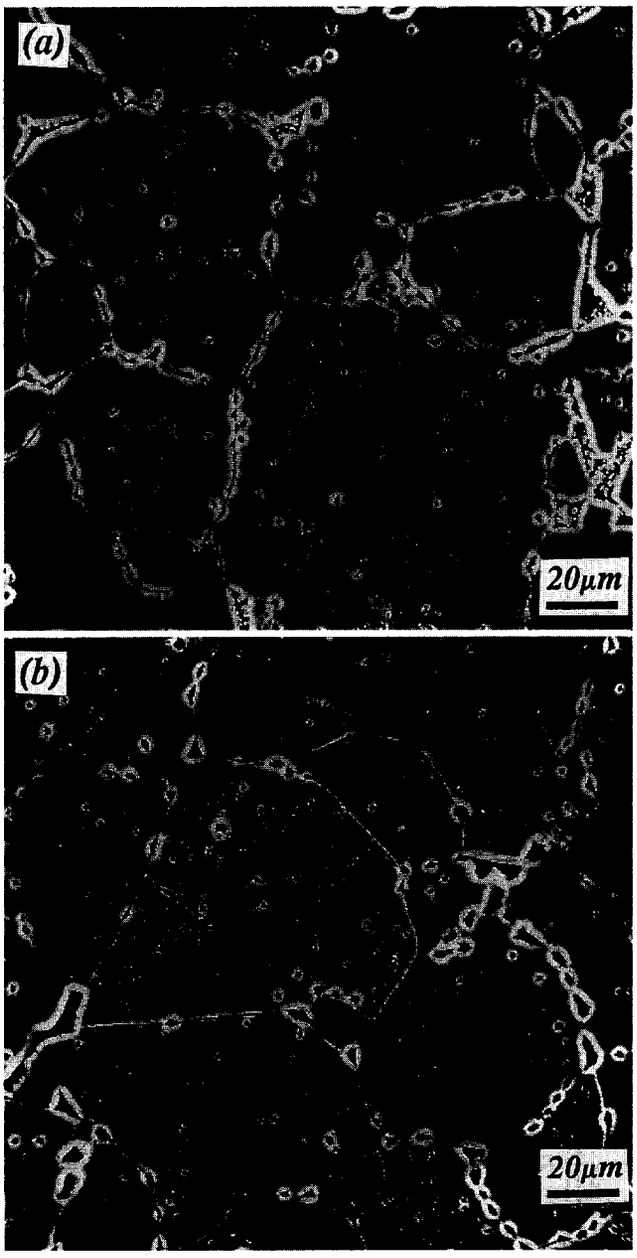

Fig. 4. High magnification (SEM) micrograph of polished and chemically etched (H_3PO_4—6 min) surfaces of samples prepared from powders attrition milled in ethyl alcohol in which different kinds of porosity are observed. (a) SP and (b) SPA-II.

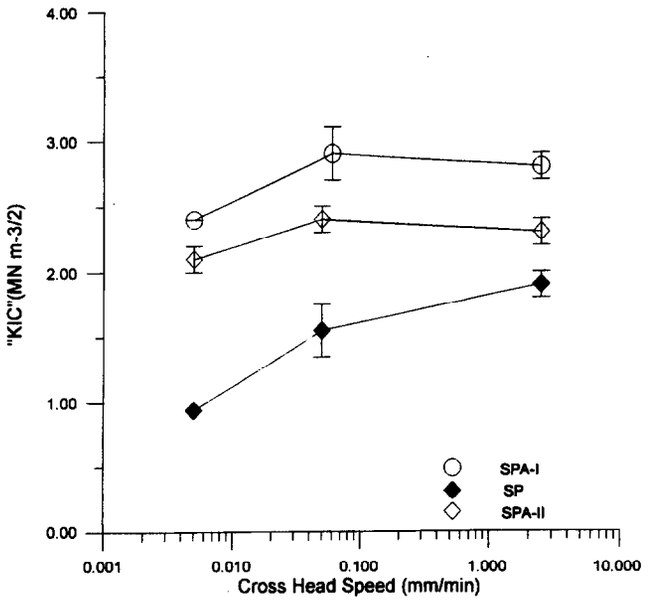

Fig. 5. Apparent toughness, 'K_{IC}', at 1200°C as a function of the cross head speed for SPA-I and SPA-II. Values corresponding to SP have been calculated from maximum loads in Fig. 8.

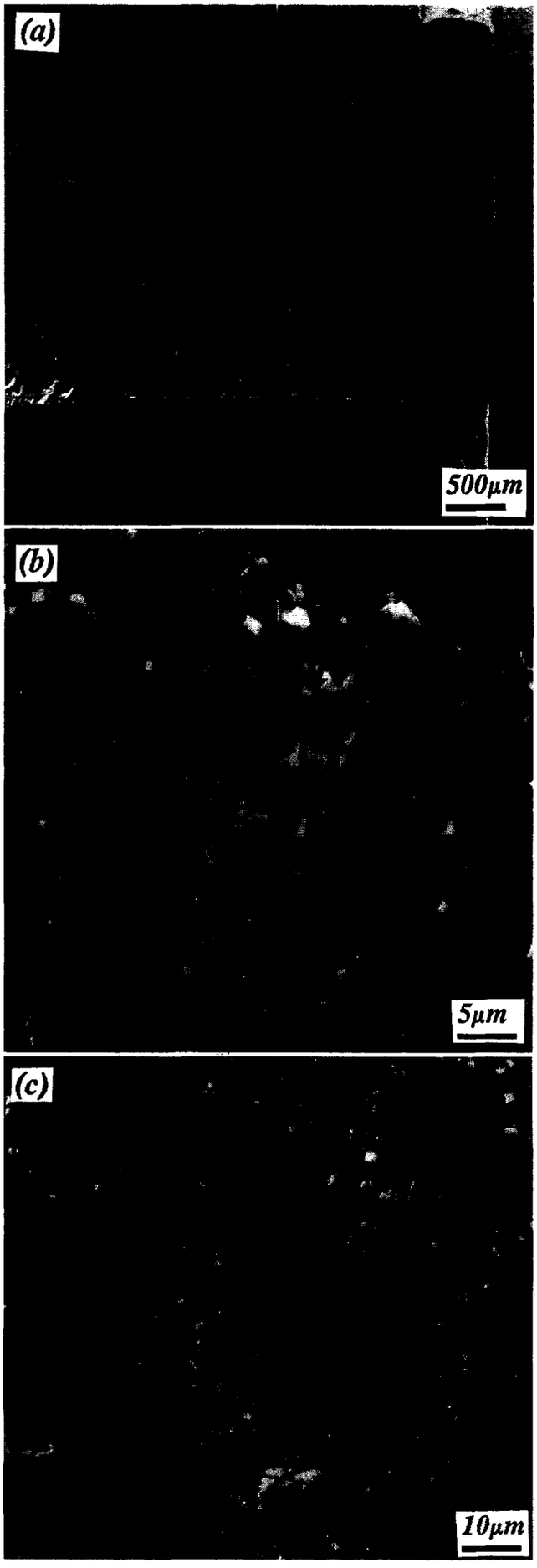

Fig. 6. Fracture surface of a toughness sample of SPA-I tested at 1200°C using a loading rate of 0·005 mm/min. (a) General view, (b) detail of the zone close to the notch, (c) detail of the centre of the surface.

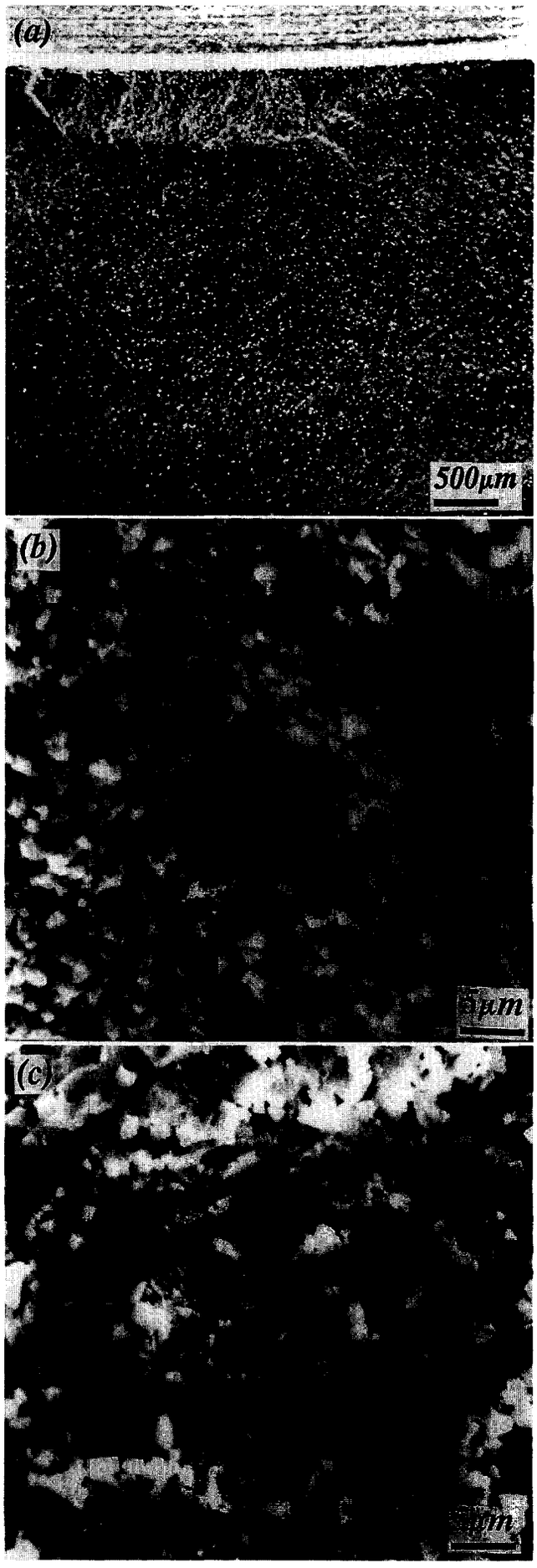

Fig. 7. Fracture surface of a toughness sample of SPA-II tested at 1200°C using a loading rate of 0·005 mm/min. (a) General view, (b) detail of the semielliptical zone close to the notch, (c) detail of the centre of the surface.

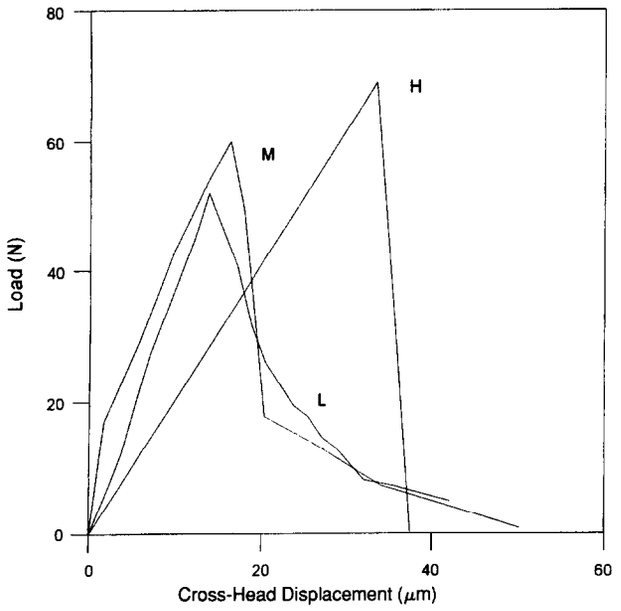

Fig. 8. Load–displacement diagrams recorded during toughness tests of SP samples performed at different loading rates: L = 0·005 mm/min, M = 0·05 mm/min, H = 2·5 mm/min.

These zones are not clearly differentiated in SPA-I (Fig. 6(a)) and apparent toughness values for this material are always higher than those for SPA-II.

When SPA-I and SPA-II are tested at higher cross-head speeds (0·05 and 2·5 mm/min) apparent toughness values are independent of strain rate (Fig. 5) and the fracture surfaces presented transgranular features such as those observed in Figs 6(c) and 7(c). The lower values of apparent toughness shown by SPA-II compared to SPA-I, when high cross-head speeds are used, must be due to the larger weakness of the spinel grains in the former material. The porous spinel grains of SPA-II (Fig. 4(b)) would be easily traversed by the crack, whereas the denser ones of SPA-I (Figs 1(b) and 3) would stand larger opposition to the crack when traversed. It is interesting to notice that the apparently weak boundaries in SPA-II, made of pore chains and necks (Fig.1(c)), were not preferential sites for crack growth when high cross-head

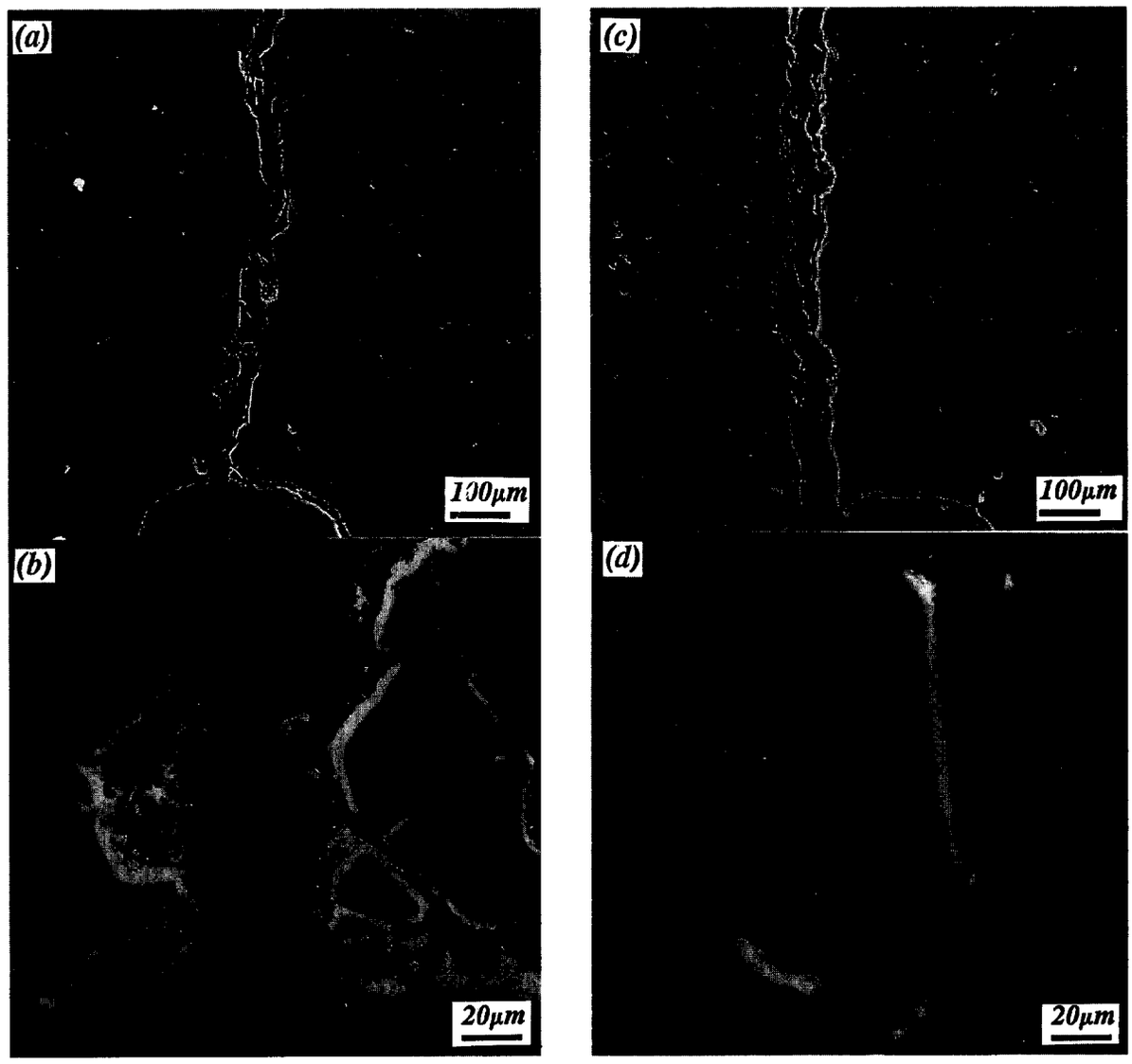

Fig. 9. Polished cross-sections of SP toughness samples tested at 1200°C. Notch area. (a, b) Loading rate = 0·05 mm/min, (c, d) loading rate = 0·005 mm/min.

speeds were used since fracture surfaces presented the same features as those shown in Fig. 7(c).

Strain rate dependence of fracture behaviour is strongly marked in SP samples in which stable fracture occurs for low cross-head speeds (Fig. 8). Even though the microstructure of SP presents the same features as that of SPA-II (Fig. 1(a,c)) the crack path in SP samples is very different from that in SPA-II samples tested using low and intermediate speeds. In the former material, fracture starts at very low stress intensities (Fig. 5), the crack runs around the large spinel grains and secondary cracking is observed (Figs 9 and 10). Moreover, SP samples tested at low and intermediate rates have stable fracture (Fig. 8) due to crack wake bridging by the large agglomerates once they have been surrounded by the crack (Figs 9 and 10).

Summarizing, the fracture behaviours at 1200°C of the studied spinels can be divided in two groups corresponding to different solid solution compositions. The stoichiometric material, SP, presents extensive subcritical crack growth across the grain boundaries for low and intermediate strain rates, whereas the alumina rich materials present this feature only at the lowest strain rate and to a very low extent. Stress intensities required for subcritical crack growth to take place in SP samples are much lower than those required in the alumina rich materials (Fig. 5). Moreover, in SP samples crack branching is observed and, due to the large size of the spinel grains, crack bridging in the wake of the main crack occurs. This division in terms of solid solution composition exists in spite of microstructural similarities between SP and SPA-II (Fig. 1(a,c)).

In previous work[1] a mechanism of crack tip yielding due to the rearrangement of lattice defects, mostly at the grain boundaries, was proposed for plasticity in a stoichiometric spinel. The considered factors responsible for plasticity in that material were cation inversion and, as proposed for deformation and superplasticity of alumina rich spinels,[6,9,14] cation vacancy formation. Formation of vacancies was related to the slight non-stoichiometry of the material and/or the presence of solid solutions of impurities such as iron oxides. In the stoichiometric material studied here these plastic phenomena do not take place,

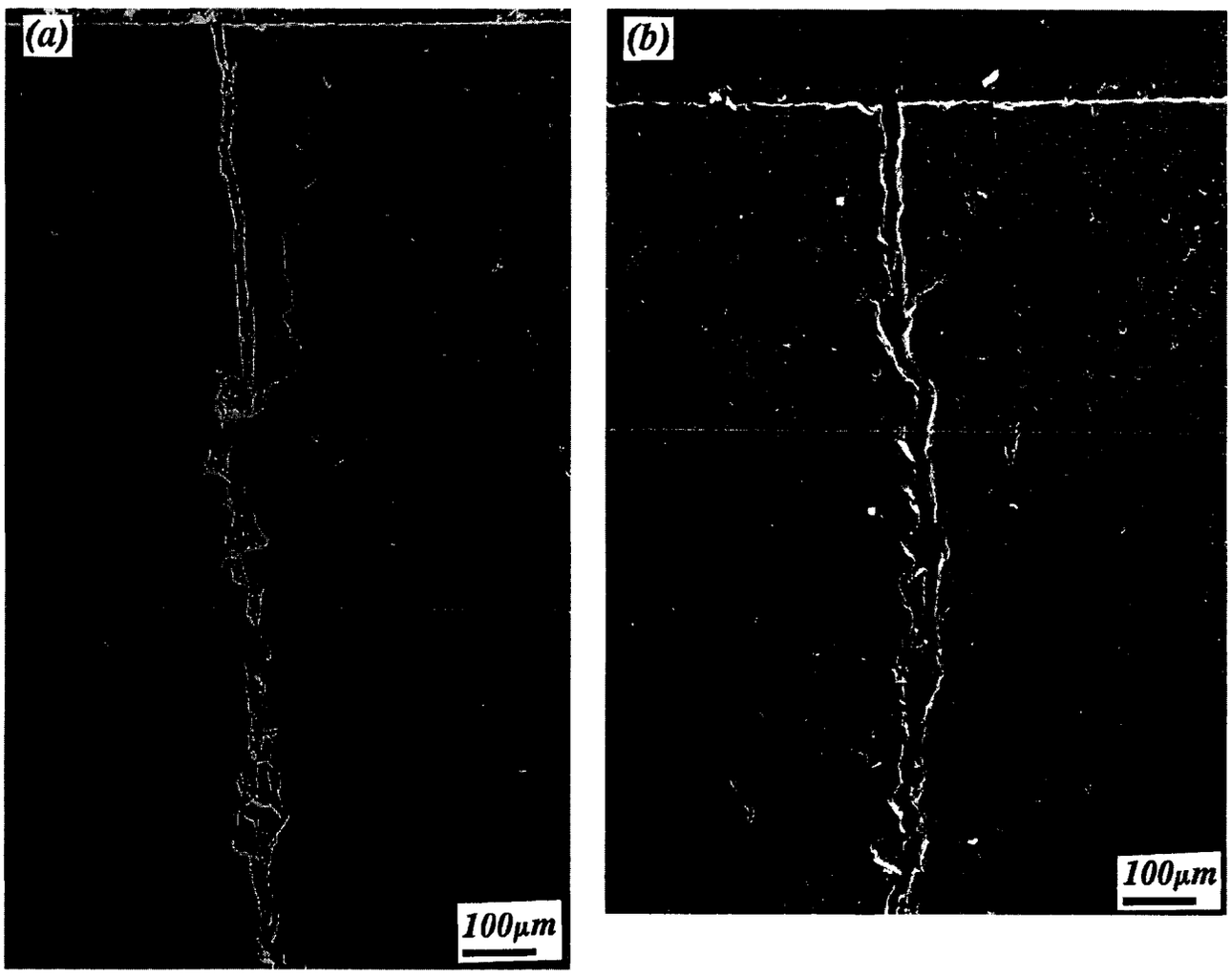

Fig. 10. Polished cross-sections of SP toughness samples tested at 1200°C. End of crack path. (a) Loading rate = 0·05 mm/min, (b) loading rate = 0·005 mm/min.

probably due to the weakness of the grain boundaries. Stress intensities required for crack propagation in the previously studied stoichiometric spinel material (~3 MN $m^{-3/2}$)[1] are larger than those determined for the material studied here, SP, (0·8–1·5 MN $m^{-3/2}$, Fig. 5). Due to the low stress intensities required for crack propagation in SP samples, brittle fracture takes place before stresses required for plastic deformation are reached.

Microstructures of SP and SPA-II are similar in terms of porosity, grain size and grain boundaries as mentioned above. Conversely, stress intensities for crack propagation are larger, the extent of subcritical crack growth is smaller and transgranular fracture dominates in SPA-II if compared to SP (Figs 5, 7 and 9). The characteristic that differentiates these two materials must be grain boundary microchemistry. Alumina solution in spinel occurs via cation vacancy formation following:[13]

$$Al_2O_3 \rightarrow 5\ Al^x_{Al} + 12\ O^x_O + 3\ Al^{\cdot}_{mg} + V'''_{Al} \quad (3)$$

and, in spite of the similar microstructures of SP and SPA-II, a larger defect concentration at SPA-II grain boundaries must exist. The presence of a large vacancy concentration in alumina rich spinels is known as a factor for enhanced plasticity. Plasticity at the grain boundaries in this material will lead to partial densification or crack blunting at the initial stages of fracture and, therefore, subcritical crack growth across grain boundaries will be inhibited. The fact that transgranular fracture dominates in these samples indicates that plastic effects occur mainly at the grain boundaries and not across the grains, probably due to the larger defect concentration at grain boundaries.

The fracture behaviour of SPA-I is similar to that of SPA-II but stress intensities required for crack propagation in SPA-I are larger (Fig. 5). Two microstructural features might be responsible for this difference in toughness: the larger availability of grain boundaries for plastic deformation and the higher toughness of the homogeneously distributed denser spinel grains in SPA-I if compared to SPA-II (Figs 1(b,c) and 3).

In other works, a mechanism of plasticity for alumina rich spinels via kinetic precipitation of alumina at the grain boundaries[8] has been proposed. The reported experiments involved alumina rich spinels tested at temperatures close to the solvus and kinetic precipitation was supported by observations of alumina precipitates at grain boundaries in tested samples. The annealing times required to detect Al_2O_3 precipitation in alumina rich spinels at 1200°C are about 10^4 s (SEM and XRD[3]) and 400 s (TEM[15]). These times are much larger than the testing times used in the present work and, therefore, kinetic crystallization is not likely to take place in SPA-I and SPA-II under the experimental conditions used here.

5 Conclusions

Three single phase spinel materials have been obtained. Two of them have different spinel solid solution composition, $MgO{\cdot}1{\cdot}02Al_2O_3$ and $MgO{\cdot}1{\cdot}96Al_2O_3$, and similar microstructural features: large porous spinel grains surrounded by pore chains. The third material has a bimodal microstructure made of highly dense spinel grains in a porous matrix and a spinel solid solution composition $MgO{\cdot}1{\cdot}98Al_2O_3$.

The fracture behaviour at 1200°C of these stoichiometric and alumina rich polycrystalline spinels is determined by the solid solution composition in spite of microstructural similarities between materials with different stoichiometry:

(i) The stress intensities at the onset of fracture in the stoichiometric material are much lower than those in the alumina rich ones.
(ii) Fracture of the stoichiometric material is mainly intergranular. This material presents extensive subcritical crack growth across the grain boundaries, crack branching and crack wake bridging for low and intermediate strain rates.
(iii) The alumina rich materials present mainly transgranular fracture and limited subcritical crack growth only when tested at the lowest strain rate.

The differences in mechanical behaviour can be related to grain boundary microchemistry as in the alumina rich materials a larger vacancy concentration will lead to grain boundary reinforcement via plastic deformation.

Acknowledgement

This work has been supported by CICYT (Spain), Contract MAT92-499.

References

1. Baudín, C., Martínez, R. and Pena, P., High temperature mechanical behavior of stoichiometric magnesium spinel. *J. Am. Ceram. Soc.*, 1995, **78**(7), 1857–1862.
2. Hallstedt, B., Thermodynamic assessment of the system $MgO–Al_2O_3$. *J. Am. Ceram. Soc.*, 1992, **75**(6), 1497–1507.
3. Panda, P. C. and Raj, R., Kinetics of precipitation of α-Al_2O_3 in polycrystalline supersaturated $MgO{\cdot}2Al_2O_3$ spinel solid solution. *J. Am. Ceram. Soc.*, 1986, **69**(5), 365–373.

4. Doukhan, N., Duclos, R. and Escaig, B., Influence of the stoichiometry on the mechanical properties of spinel $(Al_2O_3)_nMgO$ single crystals. *J. de Physique*, 1976, **37**(12), C7-566–C7-571.
5. Mitchell, T. E., Hwang, L. and Heuer, A. H., Deformation in spinel. *J. Mater. Sci.*, 1976, **11**, 264–272.
6. Becher, P. F., Press-forged Al_2O_3-rich spinel crystals for IR applications. *Am. Ceram. Soc. Bull.*, 1977, **56**(11), 1015–1017.
7. Radford, K. C., and Newey, C. W. A., Plastic deformation in magnesium-aluminate spinel. In *Proc. Br. Ceram. Soc.*, Vol. 9. The British Ceramic Society, Stoke-on-Trent, UK, 1967, pp. 131–155.
8. Panda, P. C., Raj, R. and Morgan, P. E. D., Superplastic deformation in fine-grained $MgO{\cdot}2Al_2O_3$ spinel. *J. Am. Ceram. Soc.*, 1985, **68**(10), 522–529.
9. Maguire, E. A. Jr and Gentilman, R. L., Press forging small domes of spinel. *Am. Ceram. Soc. Bull.*, 1981, **60**(2), 255–256.
10. Powder Diffraction File Databook, N.B.S. Monograph (U.S.), 25 Sec. 9 No. 21-1152. International Centre for Diffraction Data, Pennsylvania, USA, 1971.
11. Srawley, J. E. and Gross, B. In *Fracture Toughness Testing*. ASTM STP601, American Ceramic Society for Testing and Materials, Philadelphia, PA, 1976, pp. 559–579.
12. Stewart, R. L., Iwasa, M. and Bradt, R. C., Room temperature K_{IC} values for single-crystal and polycrystalline $MgAl_2O_4$. *J. Am. Ceram. Soc.*, 1981, **64**(2), C-22–C-23.
13. Chiang, Y. M. and Kingery, W. D., Grain-boundary migration in nonstoichiometric solid solutions of magnesium aluminate spinel. II: Effects of grain boundary nonstoichiometry. *J. Am. Ceram. Soc.*, 1990, **73**(5), 1153–1158.
14. Dulcos, R., Doukhan, N. and Escaig, B., Study of the origin of the composition influence on the mechanical properties of $MgO{\cdot}nAl_2O_3$ spinels. *Acta Metall.*, 1982, **30**, 1381–1388.
15. Dontlon, W. T., Mitchell, T. E. and Heuer, A. H., Precipitation in non-stoichiometric spinel. *J. Mater. Sci.*, 1982, **17**, 1389–1397.